

The C-terminal Region of D-DT Regulates Molecular Recognition for Protein–Ligand Complexes

Andrew Parkins, Aliyah Veronica R. Pilien, Alexander M. Wolff, Christopher Argueta, Jasmine Vargas, Shahrzad Sadeghi, Andreas H. Franz, Michael C. Thompson, and Georgios Pantouris*



Cite This: *J. Med. Chem.* 2024, 67, 7359–7372



Read Online

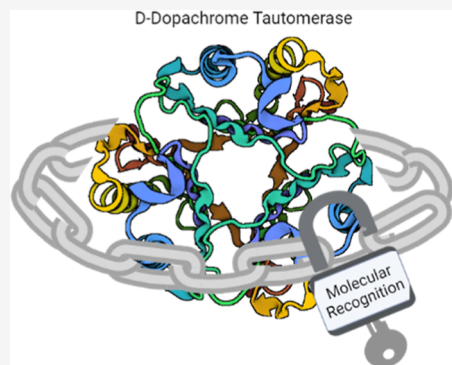
ACCESS |

Metrics & More

Article Recommendations

Supporting Information

ABSTRACT: Systematic analysis of molecular recognition is critical for understanding the biological function of macromolecules. For the immunomodulatory protein D-dopachrome tautomerase (D-DT), the mechanism of protein–ligand interactions is poorly understood. Here, 17 carefully designed protein variants and wild type (WT) D-DT were interrogated with an array of complementary techniques to elucidate the structural basis of ligand recognition. Utilization of a substrate and two selective inhibitors with distinct binding profiles offered previously unseen mechanistic insights into D-DT–ligand interactions. Our results demonstrate that the C-terminal region serves a key role in molecular recognition via regulation of the active site opening, protein–ligand interactions, and conformational flexibility of the pocket’s environment. While our study is the first comprehensive analysis of molecular recognition for D-DT, the findings reported herein promote the understanding of protein functionality and enable the design of new structure-based drug discovery projects.



INTRODUCTION

D-DT, also known as MIF-2, is a small proinflammatory cytokine¹ and enzyme² that regulates immune system responses. Encoded by chromosome 22, D-DT is primarily localized in the cytosol of several tissues and cells,^{3,4} however in response to stimulation, it is trafficked to the extracellular space or nucleus.^{1,5} The protein was originally described in 1993 as a tautomerase enzyme that converts D-dopachrome into 5,6-dihydroxyindole (DHI).⁶ Crystallographic studies performed a few years later showed that D-DT shares structural homology with the previously identified tautomerase enzyme called macrophage migration inhibitory factor (MIF).⁷ The structural and functional overlap between MIF and D-DT, as well as their adjacent gene localization, led to the premature conclusion that D-DT was a redundant protein. For this reason, all the attention of the community was given to MIF for almost two decades. However, the accumulating evidence collected over the past decade suggests a distinctive role of D-DT in human pathophysiology^{3,8–10} and promotes the need for novel mechanistic studies to understand molecular recognition of D-DT complexes.

Similar to MIF,^{11–13} D-DT binds and activates the chemokine receptor CXCR7 (ACKR3)¹⁴ and the type II cell surface receptor CD74.¹ Activation of CXCR2 by MIF, is shown to be associated with the pseudo Glu-Leu-Arg (ELR) motif of the protein,^{15,16} which in the case of D-DT is missing. Experimental findings also showed MIF to activate CXCR4^{16–18} but such knowledge is missing in the case of

D-DT. Depending on the cell type, D-DT-induced signaling is associated with multiple pathways including MAPK/ERK,^{1,19} NF-κB,²⁰ COX2/PGE₂,²¹ and AMPK.²² Activation of these pathways has a downstream effect on inflammation, cardiovascular disorders, autoimmune diseases, and cancer. While neither the structure of MIF–CD74 nor D-DT–CD74 complexes are available, structure–activity, protein dynamics, and mutational studies performed on MIF have provided key information on the MIF-induced activation of CD74.^{23–27} In contrast, D-DT experimental and computational findings related to CD74 activation are limited, and obtained in consideration of the protein’s homology with MIF.^{28–30}

Omission of the initial methionine results in a D-DT monomer that is composed of only 117 amino acids. The secondary structure of D-DT forms a four stranded β-sheet packed against two α helices.⁷ Two additional, identical subunits come together to form a globular homotrimer as the biological assembly. A pocket between adjacent monomers forms the active site of this enzyme. The tautomerase activity of D-DT is controlled by the N-terminus Proline (Pro1).^{2,6} While the biological substrate of D-DT remains unknown, D-

Received: January 21, 2024

Revised: April 13, 2024

Accepted: April 16, 2024

Published: April 26, 2024



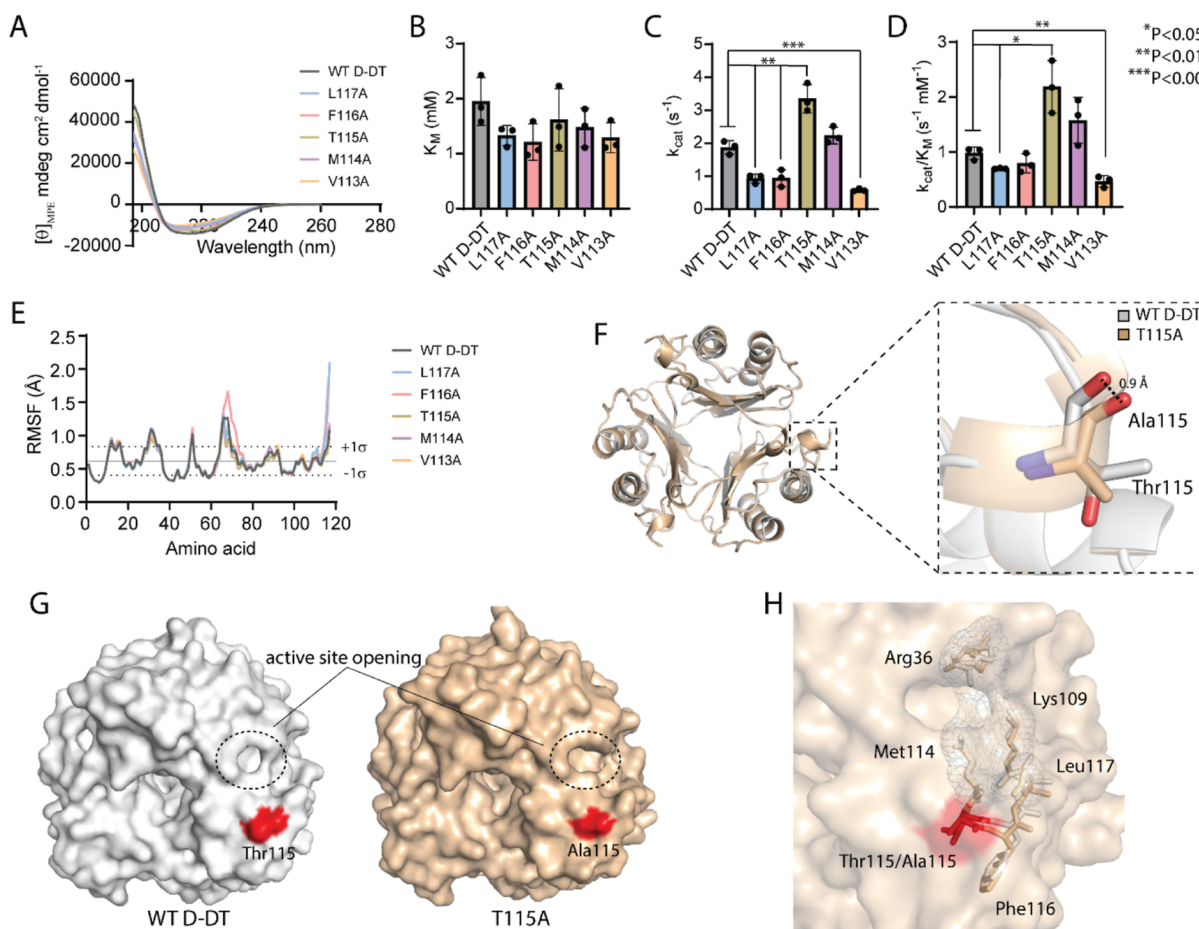


Figure 1. Biophysical, biochemical, and structural characterization of Ala variants. (A) The folding profiles of WT D-DT and the five Ala variants (L117A, F116A, T115A, M114A, and V113A) were monitored by CD spectroscopy. (B–D) Steady-state kinetic parameters of D-DT variants using 4-HPP as a substrate. The experiments were carried out in triplicate ($n = 3$) and the error values are shown as standard deviations. (E) RMSF profiles of D-DT variants were produced by 200 ns trajectories. The average RMSF value of WT D-DT (0.62 ± 0.22 Å) is shown as a solid black line. The black dashed lines represent one standard deviation ($\pm 1\sigma$) from the mean value of WT D-DT. (F) Superposition analysis of WT D-DT (light gray) and T115A (light brown) crystal structures. The point mutation caused a 0.9 Å conformational shift of residue 115. Thr115 and Ala115 are shown as light gray and light brown sticks, respectively. (G) Comparison of the active site openings for WT D-DT (light gray) and T115A (light brown). The position of Thr115 and Ala115 in the corresponding crystal structures of WT D-DT and T115A are highlighted in red. (H) Conformational changes induced by the T115A mutation (red) alter the size of the active site opening. The surface area of Arg36, Lys109, and Met114 that contributes to defining the active site opening of WT D-DT is presented as light gray mesh. The surface area of T115A is shown in light brown. Affected residues are shown as sticks. The crystal structure of WT D-DT (PDB entry: 1DPT) served as the search model for T115A (PDB entry: 8VG7).

dopachrome and 4-hydroxyphenylpyruvate (4-HPP) have been primarily used as model substrates.^{2,6,31–33} Via this enzymatic activity, four tautomerase inhibitors of D-DT have been identified thus far. The suicide inhibitor 4-iodo-6-phenylpyrimidine (4-IPP) was the first reported inhibitor of D-DT that also inhibits MIF.^{34,35} 4-IPP covalently binds to Pro1, forming a 6-phenylpyrimidine (6-PP) adduct. The first selective and reversible inhibitor of D-DT, known as 4-(3-carboxyphenyl)-2,5-pyridinedicarboxylic acid (4-CPPC), was published a few years later.³⁶ 4-CPPC binds via an induced fit mechanism that displaces the C-terminal residues Met114-Leu117, while increasing their conformational flexibility.³⁷ The conformational flexibility of this region was further investigated with molecular dynamics (MD) simulations and nuclear magnetic resonance (NMR) spectroscopy revealing structural features of D-DT that had never been observed in any prior MIF studies.³⁸ While the enhanced conformational flexibility of the C-terminal residues does not destabilize the biological assembly of D-DT, 4-CPPC may have mechanistic value for

studying the potential functional role of the C-terminal tail. Another selective and reversible inhibitor of D-DT, a derivative of thieno[2,3-*d*]pyrimidine-2,4(1H,3H)-dione, was reported to have higher potency and selectivity than 4-CPPC and was shown to inhibit the proliferation of non-small cell lung cancer (NSCLC) cells.³³ Pyridine-2,5-dicarboxylate is the most recently reported inhibitor of D-DT, and similar to the previous two, reversibly binds the active site of the protein.³⁹ Besides the fact that this molecule inhibits the D-DT-induced activation of CD74 in vivo, it also demonstrates the highest reported inhibition selectivity, 79-fold, for D-DT over MIF. The high selectivity, micromolar potency, and bioactivity make pyridine-2,5-dicarboxylate a suitable molecule for D-DT functional studies.

In this study, we utilized high resolution protein crystallography along with several complementary biophysical, biochemical, and computational methods to provide the structural basis of the D-DT–ligand complex formation. Toward this goal, we generated 17 D-DT variants and, via

their unique structural properties, investigated the mechanistic details that control ligand binding. As ligands, we employed the most commonly reported substrate, 4-HPP, and two selective inhibitors (4-CPPC and pyridine-2,5-dicarboxylate) that bind to D-DT in a distinct fashion. Our study provides the first comprehensive analysis of the structural parameters that control formation of D-DT–ligand complexes and demonstrates that the C-terminal region is a key regulator of molecular recognition via a multitier control mechanism.

■ RESULTS AND DISCUSSION

Selection of Protein Variants. Our previous work, utilizing MD simulations and NMR, revealed an enhanced flexibility of D-DT's C-terminal residues when bound to the selective and reversible inhibitor, 4-CPPC. As binding of this ligand did not compromise the biological assembly of D-DT, it raises the question of whether C-terminal conformational changes are a key aspect for molecular recognition. Thus, various mutations were made on the C-terminal residues to understand the biological significance of this flexibility.

Single point alanine (Ala) mutations were first considered. An overlay of WT D-DT (PDB entry: 1DPT) crystal structure onto the corresponding structure of D-DT–4-CPPC (PDB entry: 6CSF) revealed that Val113 was the last C-terminal residue to be drastically affected by 4-CPPC binding (Figure S1). For this reason, the single point Ala mutations were extended from C-terminus Leu117 to Val113 (L117A, F116A, T115A, M114A, and V113A).

While the Ala mutations would provide information about the potential functional role of side chains, the C-terminal glycine (Gly) mutations would aid in understanding how backbone flexibility affects the ligand recognition and dynamic coupling of residues across the biological assembly. Our previously published correlation analysis of D-DT–4-CPPC revealed that the structural flexibility of the C-terminal tail enables long-range intra/intersubunit communications across D-DT.³⁸ Whether these findings are associated with the functionality of D-DT remains unclear. Thus, the Gly variants would offer a valuable tool for exploring the relationship between protein dynamics and catalytic activity. Toward this goal, we produced four variants (L117G, L117G/F116G, L117G/F116G/T115G, and L117G/F116G/T115G/M114G). Production of poly-Gly variants stopped at Met114 considering the crystal structure of D-DT–4-CPPC, which pointed that this was the last residue with enhanced flexibility (Figure S1).³⁷

In addition to Ala and Gly variants, which provide information on the functionality of side chains and backbone, respectively, we also produced three C-terminal truncations (Δ 114–117, Δ 109–117, and Δ 104–117). These variants were carefully selected to avoid truncating any major secondary structure of D-DT (Figure S2A). The rationale for producing these variants was that a stepwise deletion of C-terminal residues would gradually increase the size of the active site opening, allowing unrestricted access to the catalytic pocket. Therefore, if conformational changes are required for ligand recognition, this would become apparent. We employed the crystal structure of WT D-DT to model the active site openings for Δ 114–117, Δ 109–117, and Δ 104–117 (Figure S2B). A side-by-side comparison of WT D-DT, and the three modeled truncations, confirmed that the size of the active site opening progressively increases from WT D-DT to Δ 104–117. Considering that these alterations would not drastically impact

the stability of the D-DT trimer, they would offer an alternative approach to explore the potential implementation of an induced-fit binding mechanism for D-DT.

Characterization of Ala Variants. Prior to the kinetic characterization of single point Ala mutants, we performed folding experiments using circular dichroism (CD) spectroscopy. The five variants (L117A, F116A, T115A, M114A, and V113A) and WT D-DT were analyzed side-by-side, demonstrating similar secondary structural profiles (Figure 1A). Following, we employed the keto–enol tautomerization assay to assess the impact of these mutations on the enzymatic activity of D-DT. For our experiments, 4-HPP was used as a substrate.³² Three biological replicates were performed, and the Michaelis–Menten parameters were analyzed (Figure 1B–D). Truncation of side chains for residues 113–117 did not have any drastic impact on the binding affinity of 4-HPP, as shown by the Michaelis constant (K_M) values (Figure 1B, Table S1). In contrast, the turnover numbers (also known as k_{cat}) were noticeably impacted (Figure 1C, Table S1). Having WT D-DT ($k_{cat} = 1.88 \pm 0.20 \text{ s}^{-1}$) as the point of reference, we observed two trends. While L117A, F116A, and V113A demonstrated a decrease in their turnover numbers, T115A showed a surprising increase. For simplicity, we converted the k_{cat} values to percent (%) change using the following formula: $[(\text{value}_{\text{variant}} - \text{value}_{\text{WT D-DT}})/\text{value}_{\text{WT D-DT}}] \times 100$. L117A and F116A with corresponding k_{cat} values of $0.93 \pm 0.14 \text{ s}^{-1}$ and $0.95 \pm 0.26 \text{ s}^{-1}$ exhibited a similar drop of ~50%. V113A, with a k_{cat} value of $0.58 \pm 0.04 \text{ s}^{-1}$, was the variant being affected the most, as shown by the 69% reduction of its turnover value. In contrast, T115A ($k_{cat} = 3.35 \pm 0.43 \text{ s}^{-1}$) increased its ability to turnover 4-HPP by 78% (Figure 1C, Table S1). The catalytic efficiencies (k_{cat}/K_M) of WT D-DT ($0.98 \pm 0.11 \text{ s}^{-1} \text{ mM}^{-1}$) and the Ala variants were also investigated (Figure 1D, Table S1). V113A ($0.46 \pm 0.10 \text{ s}^{-1} \text{ mM}^{-1}$) and T115A ($2.18 \pm 0.48 \text{ s}^{-1} \text{ mM}^{-1}$) were the two mutants that demonstrated the highest deviation from the k_{cat}/K_M value of WT D-DT. The side chain mutation of residue 113 reduced the k_{cat}/K_M value of V113A by 53%, whereas in the case of T115A, mutagenesis created a more efficient enzyme yielding an impressive increase of 122%.

We performed MD simulations to explore the effect of side chain truncations on the global (biological assembly) and local (around the point mutation) conformational flexibility of D-DT. Our analysis showed that the Ala mutants and WT D-DT have similar root-mean-square fluctuation (RMSF) values (Figure 1E, Table S2). While the average RMSF value of WT D-DT was determined at $0.62 \pm 0.22 \text{ \AA}$, the corresponding values of the five variants ranged from $0.59 \pm 0.18 \text{ \AA}$ (T115A) to $0.67 \pm 0.31 \text{ \AA}$ (F116A) (Table S2). Upon inspection of the V113A ($\text{Avg}_{\text{RMSF}} = 0.63 \pm 0.21 \text{ \AA}$) and T115A ($\text{Avg}_{\text{RMSF}} = 0.59 \pm 0.18 \text{ \AA}$) fluctuation profiles, we did not notice any substantial differences that could potentially explain the kinetic findings for these proteins (Figure 1D).

Besides the global analysis, we also explored the local dynamic effect of these mutations. Noticeable changes in local dynamics were only observed for L117A and F116A (Figure 1E). Specifically, the side chain truncations of Leu117 and Phe116 drastically increased the conformational flexibility of the C-terminal region, which was not surprising considering the position of these residues. In the case of F116A, the point mutation had an additional effect on residues 66–76, which are located proximal to the C-terminal tail (Figure 1E). Despite these differences, the kinetic findings show that L117A and

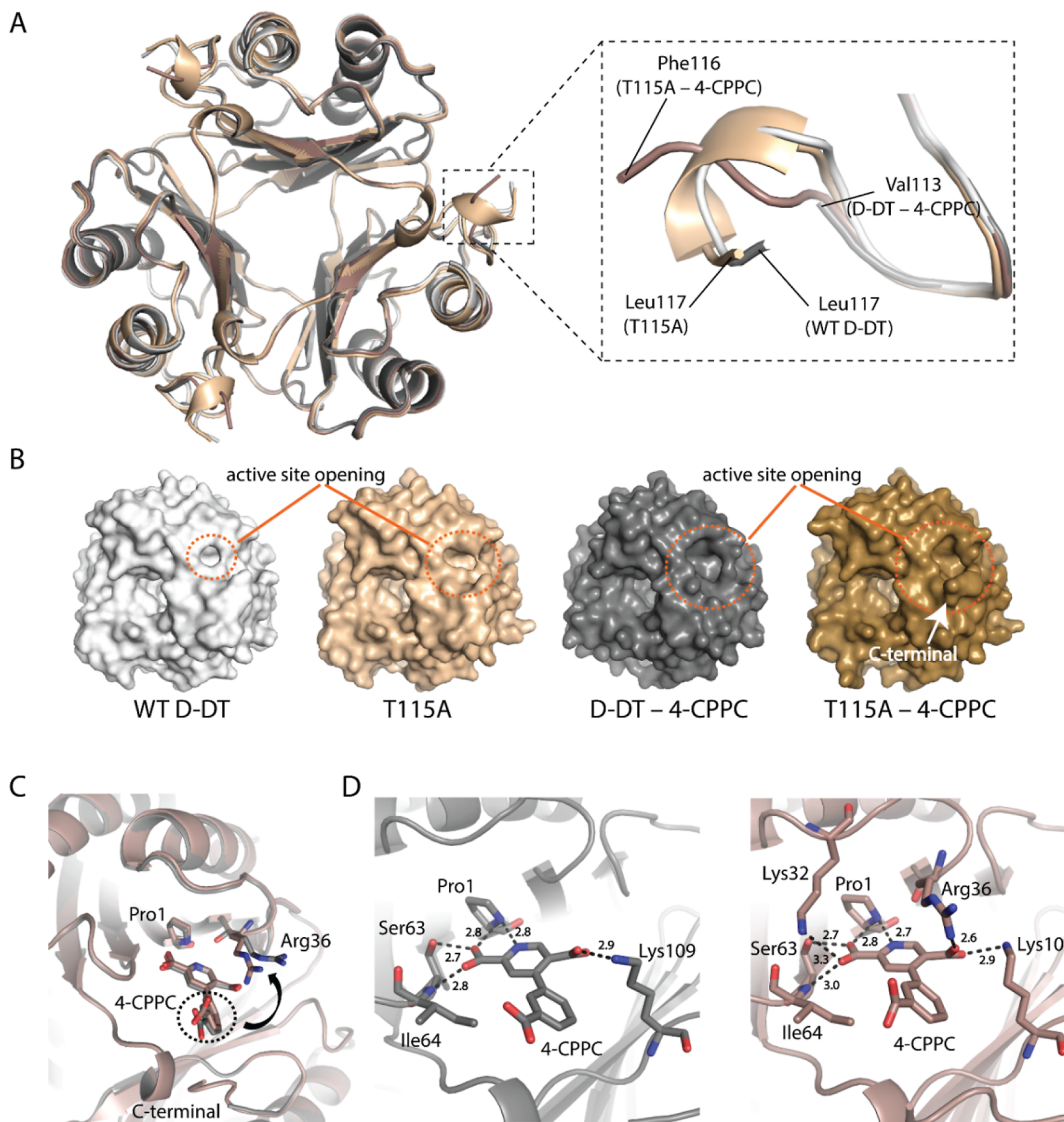


Figure 2. Crystallographic analyses of T115A and T115A-4-CPPC. (A) Evaluation of the superposition agreement between WT D-DT (light gray), T115A (light brown), D-DT-4-CPPC (dark gray), and T115A-4-CPPC (dark brown). The C-terminal region illustrates differences in the conformational flexibility of the four proteins. The C-terminus residues are pointed with solid lines. (B) Side-by-side comparison of the active site openings (orange dashed circles) of the four D-DT variants. The C-terminal region of T115A-4-CPPC is pointed with a white arrow. (C) Conformational changes of 4-CPPC's benzoic ring (dashed circle) affect the conformation of the active site residue Arg36 (black arrow). Pro1, Arg36 and 4-CPPC from the crystal structures of D-DT-4-CPPC (dark gray), and T115A-4-CPPC (dark brown) are shown as sticks. (D) Hydrogen bonding interactions (dashed lines) between active site residues and 4-CPPC, as noted in the crystal structures of D-DT-4-CPPC (left) and T115A-4-CPPC (right). Hydrogen bonding distances are shown in angstrom (\AA). The crystal structure of WT D-DT (PDB entry: 1DPT) served as the search model for T115A (PDB entry: 8VG7) and T115A-4-CPPC (PDB entry: 8VG8).

F116A are two variants of low interest (Figure 1D). Collectively, our findings support that alteration of protein dynamics, due to side chain truncation, did not have any drastic effect on the catalytic activities of the Ala variants.

Role of Residue 115 in Molecular Recognition. T115A was crystallized and structurally inspected, considering that it was the C-terminal variant with the most substantial impact on the catalytic activity of D-DT (Table S3). Overlay of T115A crystal structure onto WT D-DT (PDB entry: 1DPT) revealed a high superposition agreement with a root-mean-square deviation (rmsd) value of 0.33 \AA (Figure 1F, Table S4). Closer inspection of the mutated residue exposed a conformational change of 0.9 \AA (Figure 1F), which at first glance appears to be insignificant. However, surface analysis showed that this small shift of residue's 115 position had a notable

impact on the size and shape of active site's opening (Figure 1G). In turn, this is explained by conformational changes in residues found surrounding Ala115 (Figure 1H). Upon Ala115 backbone movement, residues Arg36, Lys109, and Met114 adopt distinct side chain conformations that increase the size of the active site opening (Figure 1H). Phe116 and Leu117 are also affected by the T115A mutation, but their conformational changes do not have any direct impact on the opening of the active site.

To extend our understanding, we employed two selective D-DT inhibitors, 4-CPPC and pyridine-2,5-dicarboxylate, to carry out inhibition assays for WT D-DT and T115A. For reference, the previously reported inhibition constant (K_i) values of 4-CPPC and pyridine-2,5-dicarboxylate for WT D-DT are $33 \pm 0.7 \mu\text{M}^{37}$ and $17.2 \pm 0.9 \mu\text{M}^{39}$, respectively. Notably, pyridine-

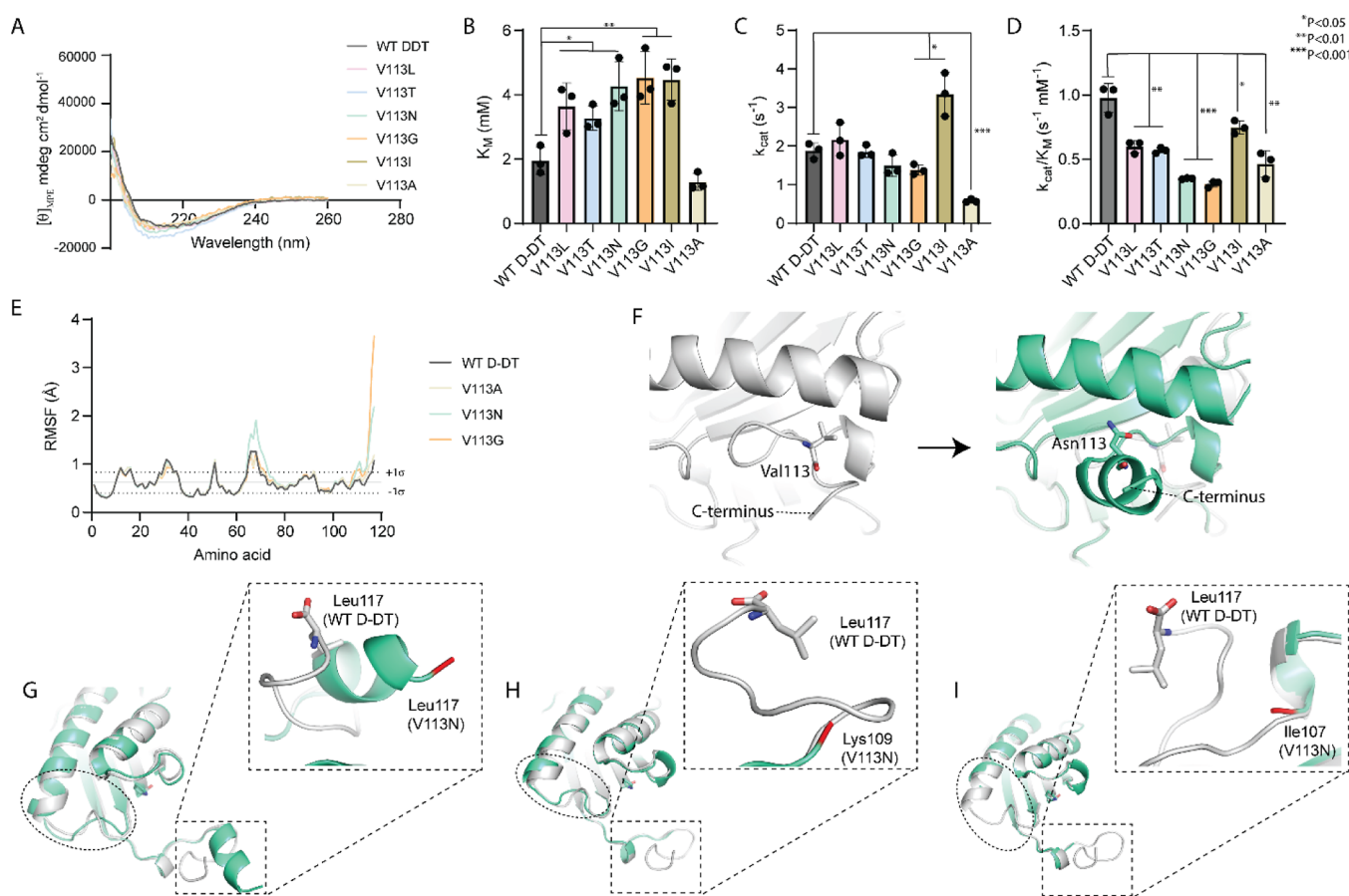


Figure 3. Impact of Val113 mutation on the structure and function of D-DT. (A) The folding profiles of WT D-DT and the six Val113 variants (V113L, V113T, V113N, V113G, V113I, and V113A) were plotted and compared. (B–D) Impact of Val113 mutagenesis on the Michaelis–Menten parameters of D-DT. The experiments were carried out in triplicate ($n = 3$) and the error values are shown as standard deviations. (E) Comparison of the RMSF profiles for WT D-DT and the three Val113 variants (V113A, V113N, and V113G) with the smallest k_{cat}/K_M values. The black dashed lines represent one standard deviation ($\pm 1\sigma$) from the mean value of WT D-DT (black solid line). (F) The crystal structures of WT D-DT (left, gray) and V113N (right, green) were examined, side-by-side, to evaluate the structural impact of V113N mutation. On the right, an overlay of WT D-DT (transparent gray) onto V113N demonstrates the original position of residue 113, C-terminal tail, and the surrounding environment before the mutation. Val113 and Asn113 are shown as sticks. (G–I) The three subunits of WT D-DT (gray) and V113N (green) were superimposed and compared to observe structural differences associated with the V113N mutation. For each subunit of V113N, the terminus residue is highlighted in red. Leu117, which is the terminus amino acid of WT D-DT, is shown as sticks. The dashed ovals and boxes illustrate conformational differences noted, between WT D-DT and V113N crystal structures, in the 64–77 segment ($\beta 4/\alpha 2$ loop and $\alpha 2$ helix) and C-terminal region, respectively. The crystal structure of WT D-DT (PDB entry: 1DPT) served as the search model for V113N (PDB entry: 8VFW).

2,5-dicarboxylate is a derivative of 4-CPPC that demonstrates enhanced inhibition selectivity and potency, over the maternal molecule.³⁹ Despite their structural similarities, we anticipated that utilizing both inhibitors would be valuable for understanding the mechanism of recognition by D-DT, since they each have a distinct impact on the C-terminal residues. For 4-CPPC, formation of the protein-inhibitor complex is associated with major conformational changes of the C-terminal region.³⁷ Contrary to 4-CPPC, binding of pyridine-2,5-dicarboxylate does not affect the conformation of the C-terminal residues.³⁹ In the presence of 4-CPPC, the corresponding K_i values of WT D-DT and T115A were determined at $37.7 \pm 5.6 \mu\text{M}$ and $36.4 \pm 3.3 \mu\text{M}$ (Figure S3). For pyridine-2,5-dicarboxylate, the K_i values of $17.1 \pm 0.2 \mu\text{M}$ and $18.5 \pm 1.2 \mu\text{M}$ were obtained for WT D-DT and T115A, respectively (Figure S4). Our findings confirmed previously published K_i values of 4-CPPC³⁷ and pyridine-2,5-dicarboxylate³⁹ against WT D-DT and demonstrated that the single point mutation of Thr115 had neither a beneficial, nor detrimental, effect on the inhibition potencies of these two inhibitors.

We cocrystallized T115A–4-CPPC (Table S3) to examine the structural details of these interactions. With the crystallographic findings of D-DT–4-CPPC in mind,³⁷ we considered this ligand as the best one to investigate the molecular recognition features of D-DT. Alignment of T115A–4-CPPC onto the crystal structures of WT D-DT, T115A, and D-DT–4-CPPC (PDB entry: 6C5F) demonstrated high superposition agreement with rmsd values of 0.17, 0.29, and 0.23 Å, respectively (Figure 2A, Table S4). In the absence of global structural differences, we focused on the local impact that 4-CPPC had on the C-terminal residues and the opening of the active site. A close inspection of the T115A–4-CPPC C-terminal region revealed electron density up to Phe116. Upon binding of 4-CPPC, the C-terminal tail of T115A adopts a unique conformation that noticeably differs from those of WT D-DT, apo T115A, and D-DT–4-CPPC (Figure 2A). Surface analysis, with an emphasis on the catalytic pocket, demonstrated similar active site openings for D-DT–4-CPPC and T115A–4-CPPC yet remarkably different surface scaffolds (Figure 2B). These differences are associated with C-terminal

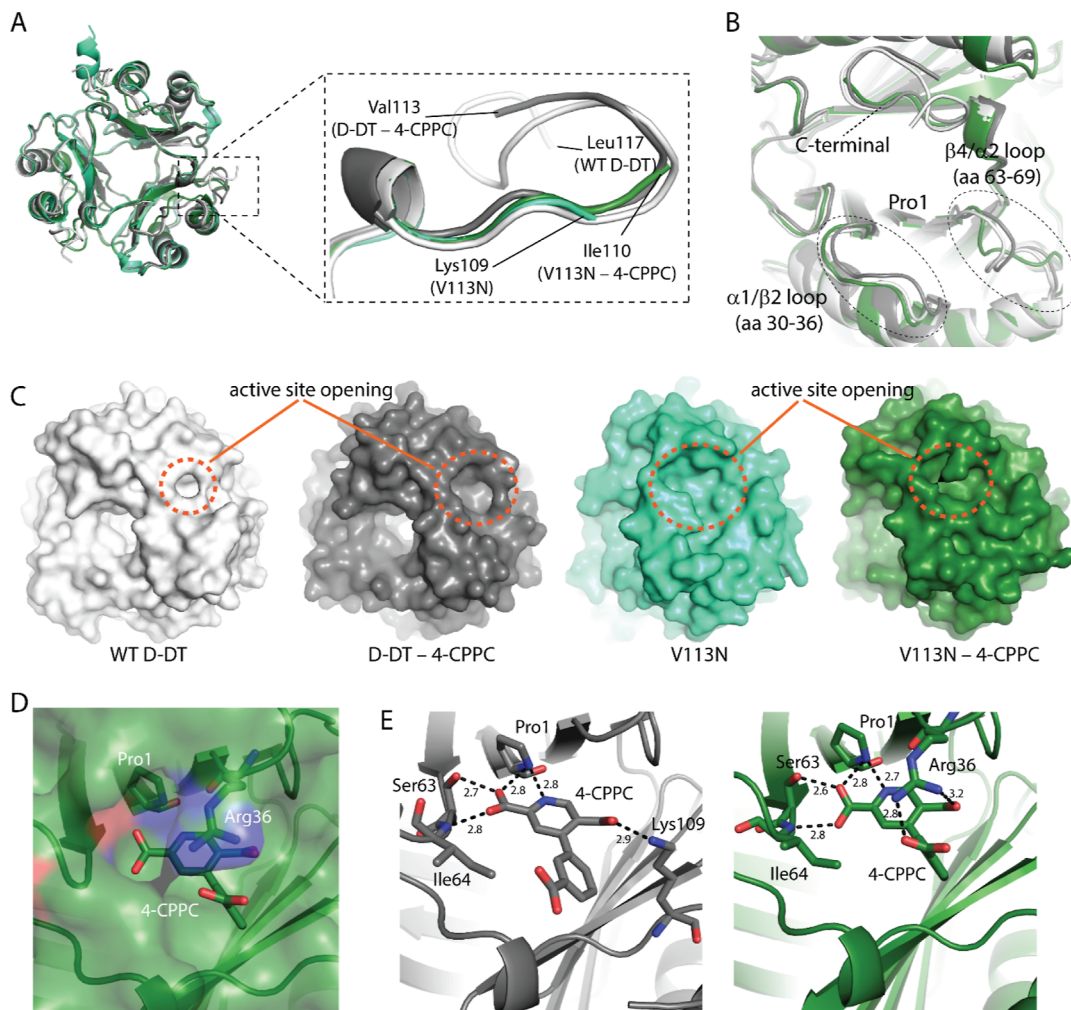


Figure 4. Crystallographic analyses of V113N and V113N-4-CPPC. (A) The crystal structures of WT D-DT (light gray), D-DT-4-CPPC (dark gray), V113N (green), and V113N-4-CPPC (dark green) were superimposed and compared. Structural differences at the C-terminal region are illustrated. The terminus residue for each protein is pointed by solid lines. (B) The increased conformational flexibility of the C-terminal tail has an impact on the α_1/β_2 and β_4/α_2 loops of D-DT (dashed ovals). (C) Comparison of the active site opening (orange dashed circles) of WT D-DT, D-DT-4-CPPC, V113N, and V113N-4-CPPC. (D) Upon binding of 4-CPPC, Arg36 adopts a new conformation that “locks” the ligand in the active site of V113N. Pro1, Arg36, and 4-CPPC are shown as sticks. (E) Analysis of the hydrogen bonding interactions (dashed lines) between D-DT and 4-CPPC (sticks), as noted in the crystal structures of D-DT-4-CPPC (left) and V113N-4-CPPC (right). Hydrogen bonding distances are shown in angstrom (\AA). The active site residues involved in hydrogen bonding interactions are shown as sticks. The crystal structure of WT D-DT (PDB entry: 1DPT) served as the search model for V113N (PDB entry: 8VFW) and V113N-4-CPPC (8VG5).

residues 114–116, which are missing from the D-DT-4-CPPC crystal structure but are present in the structure of T115A-4-CPPC (Figure 2A).

Analyzing the binding motif of 4-CPPC in the active sites of D-DT-4-CPPC and T115A-4-CPPC, we observed key differences that expose previously unseen molecular recognition features of D-DT. The C-terminal residues 114–116 (T115A-4-CPPC) force the benzoic moiety of 4-CPPC to alter its conformation (Figure 2C). Upon this movement, Arg36 undergoes a conformational shift to form a strong hydrogen bonding interaction (H-bond) with the 5-carboxylate group of the molecule’s pyridine ring. Notably, the H-bond of 4-CPPC with Arg36 is not observed in the D-DT-4-CPPC structure (Figure 2D). Considering the role of Arg36 in regulating the size of the active site opening, we conclude that formation of a 2.6 \AA H-bond “locks” 4-CPPC in the active site of D-DT. In addition to Arg36, Lys32 was also noted to form a 3.3 \AA H-bond with the 2-carboxylate group of the pyridine ring. While all the hydrogen bonding interactions observed in

the crystal structure of D-DT-4-CPPC are retained in T115A-4-CPPC, the additional H-bonds observed with Arg36 and Lys32 are clearly C-terminal induced.

Role of Residue 113 in Molecular Recognition.

Following up on the kinetic data of V113A, we probed answers regarding the poor turnover number and catalytic efficiency of this specific mutant (Figure 1C,D). While Val113 is packed in a hydrophobic pocket formed between the α_2 helix and the C-terminal 3.6 helix, we considered selective mutations that would potentially provide mechanistic insights. First, we mutated valine to leucine (V113L), isoleucine (V113I), and asparagine (V113N). The rationale behind these mutations was that they would alter the packing properties of residue 113. Besides packing, V113N would also offer information regarding the role of side chain’s hydrophobicity. Following, we produced V113T. This variant would alter the hydrophobic character on the side chain without altering the packing properties of the residue. Lastly,

we produced V113G anticipating that this variant would provide information about the role of backbone flexibility.

The folding profiles of V113G, V113L, V113I, V113T, V113N, and V113A were examined side-by-side with WT D-DT (**Figure 3A**). While this analysis did not demonstrate any outliers, we proceeded with the kinetic characterization of all variants. Side chain modifications of residue 113 had a noticeable impact on the affinity of D-DT for 4-HPP, as shown by the K_M results (**Figure 3B, Table S1**). Apart from V113A, all of the remaining variants displayed an increase of their K_M values. The highest deviation from the K_M value of WT D-DT was noted with V113G, V113I, and V113N, which exhibited an increase in the range of 120–130% (**Table S1**). These results support the notion that alterations of the packing, flexibility, and/or hydrophobicity of residue 113 have a negative impact on the affinity of D-DT for its substrate. In contrast to the K_M values, the turnover numbers of Val113 variants were not drastically affected except for V113G (26% decrease), V113I (78% increase), and V113A (69% decrease) (**Figure 3C, Table S1**). Overall, the k_{cat}/K_M values of all variants reduced (**Figure 3D, Table S1**). V113N and V113G demonstrated the highest deviation from the k_{cat}/K_M value of WT D-DT with corresponding reductions of 64 and 68%.

Selecting the three variants with the smallest k_{cat}/K_M values (V113N, V113G, and V113A), we performed 200 ns MD simulations and plotted their RMSF profiles (**Figure 3E, Table S2**). Our approach aimed to display dynamic features of these variants that would potentially explain the kinetic findings. While the average RMSF values of these variants were similar to that of WT D-DT (**Table S2**), we focused on the local environment of the C-terminal region. Mutation of Val113 to either asparagine or glycine enhanced the conformational flexibility of C-terminal residues 108–117, while V113A did not display noticeable differences from WT D-DT (**Figure 3E**). In the case of V113N, we also observed an elevated fluctuation for residues 64–77. These residues are located on the $\beta 4/\alpha 2$ loop and $\alpha 2$ helix, which in turn are found in close proximity to the C-terminal region of the adjacent monomer.

From the kinetic (**Figure 3B–D**) and protein dynamics (**Figure 3E**) analyses, V113N appears as the variant with the most interesting features. For this reason, we performed protein crystallography to obtain structural insights into this variant (**Table S5**). Superposition analysis of V113N onto the crystal structure of WT D-DT yielded an rmsd of 0.54 Å (**Table S4**). Upon closer inspection, the Val113 to Asn mutation displaced the residue from its hydrophobic pocket (**Figure 3F–G**) and increased the C-terminal flexibility (**Figure 3G–I**). From a protein crystallography perspective, this statement is supported by either the lack of electron density for the affected region or a structural conformation that significantly differs from the corresponding conformation of WT D-DT. Conformational changes in the C-terminal region were observed in one of the three subunits of V113N (**Figure 3G**). For this subunit, the electron density was clearly observed up to the C-terminus residue, Leu117. In contrast, the remaining two subunits possessed incomplete electron densities of their C-terminal regions. For subunits two and three, Lys109 (**Figure 3H**) and Ile107 (**Figure 3I**) were the last amino acids with complete electron density. In agreement with the MD simulations, WT D-DT and V113N exhibited remarkable differences in the dynamic profiles of residues 64–77 (**Figure 3G–I**). In one of the subunits of V113N, the electron density of residues 65–72 was missing (**Figure 3I**).

To associate the crystallographic findings of V113N with functional insights, we performed inhibition studies of WT D-DT and V113N in the presence of either 4-CPPC or pyridine-2,5-dicarboxylate. As shown by the inhibition constants of $37.7 \pm 5.6 \mu\text{M}$ (WT D-DT) and $58.1 \pm 3.4 \mu\text{M}$ (V113N), the Val to Asn point mutation did not have a strong impact on the inhibition potency of 4-CPPC (**Figure S5**). However, the inhibition studies of pyridine-2,5-dicarboxylate led to an opposite conclusion. With reference to WT D-DT findings ($17.1 \pm 0.2 \mu\text{M}$), the inhibition potency of pyridine-2,5-dicarboxylate against V113N essentially vanished at $397 \pm 31 \mu\text{M}$ (**Figure S6**).

We crystallized V113N with 4-CPPC (**Table S5**) and aligned it onto the crystal structures of WT D-DT, V113N, and D-DT–4-CPPC (**Figure 4A**). Superposition agreement between the various structures ranged from 0.48 to 0.63 Å (**Table S4**). The highest superposition agreement of 0.48 Å was noted between the crystal structures of V113N–4CPPC and V113N, while the lowest agreement of 0.63 Å was observed between V113N–4CPPC and D-DT–4CPPC. Diverse dynamic profiles of the C-terminal tail were noted upon inspection of the four crystal structures with V113N, V113N–4CPPC, and D-DT–4CPPC being characterized by increased conformational flexibility in comparison to WT D-DT (**Figure 4A**).

This enhanced flexibility had a clear impact on the $\alpha 1/\beta 2$ (residues 30–36) and $\beta 4/\alpha 2$ (residues 63–69) loops, which are located proximal to the C-terminal tail (**Figure 4B**). Comparison of the active site opening of the four proteins fully explains the inhibition findings obtained for 4-CPPC and pyridine-2,5-dicarboxylate. The highly flexible C-terminal region, which is enabled by the V113N mutation, alters the surface scaffold around the active site and converts the binding pocket to a groove (**Figure 4C**). Such architectural alteration cannot effectively retain pyridine-2,5-dicarboxylate bound to D-DT. In addition, the increased flexibility of Lys109 did not promote the stabilization of the protein–ligand complex. As noted in the crystal structure of D-DT–pyridine-2,5-dicarboxylate,³⁹ Lys109 forms a 2.8 Å hydrogen bonding interaction with the 5-carboxylate group of the molecule. This bond is likely abolished in the case of the V113N variant.

In-depth inspection of V113N–4CPPC revealed previously unrecognized structural features of D-DT. When the inhibitor binds to V113N, Arg36 adopts a novel conformation that “locks” 4-CPPC in the active site pocket (**Figure 4D**). This conformation of Arg36 enables hydrogen bonding interactions with two of the carboxylate groups of 4-CPPC and supports stabilization of the protein–ligand complex (**Figure 4E**). The 2.8 Å H-bond formed between the benzoic moiety of 4-CPPC and Arg36 has not been observed in any of the earlier analyzed protein–inhibitor crystal structures and offers a fresh perspective of molecular recognition.

Characterization of Gly Variants. To evaluate the role of backbone flexibility in molecular recognition, we first examined whether any regions of D-DT, including the C-terminal tail, are inherently flexible. The crystal structures of WT D-DT, obtained at 290 and 310 K (**Table S6**), were aligned onto the previously published, cryo structure of WT D-DT (PDB entry: 7MSE—100 K). The rmsd values of 0.21 Å (WT D-DT—290 K) and 0.24 Å (WT D-DT—310 K) demonstrate high superposition agreement with WT D-DT (**Figure S7, Table S4**). Neither the C-terminal tail nor any other region of D-DT revealed spontaneous flexibility at higher temperatures.

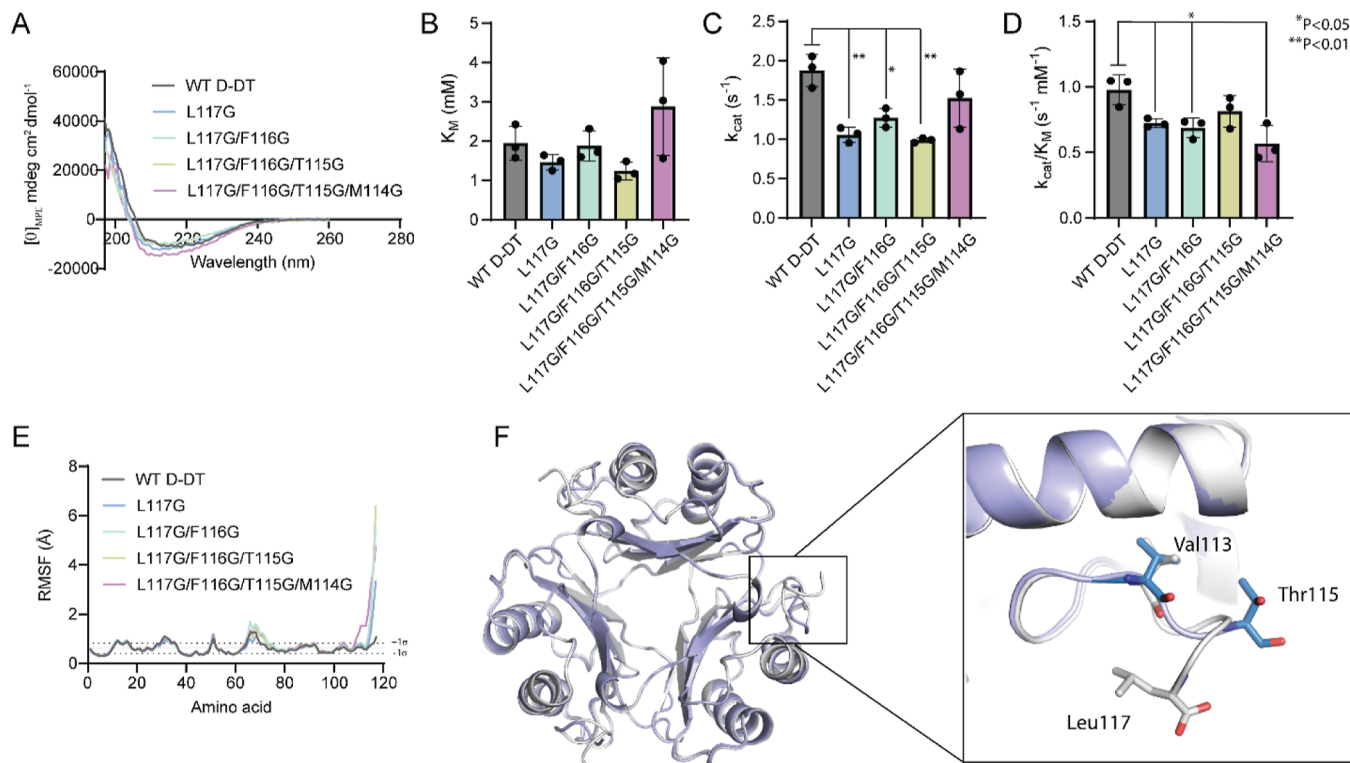


Figure 5. Characterization of Gly variants. (A) Folding profiles of WT D-DT and the four Gly variants (L117G, L117G/F116G, L117G/F116G/T115G, and L117G/F116G/T115G/M114G). (B–D) Michaelis–Menten parameters of WT D-DT and the Gly variants. The experiments were carried out in triplicate ($n = 3$) and the error values are shown as standard deviations. (E) RMSF profiles of WT D-DT and Gly variants. The black dashed lines represent one standard deviation ($\pm 1\sigma$) from the mean value of WT D-DT (black solid line). (F) Superposition analysis of the crystal structures of WT D-DT (light gray) and L117G are shown as sticks. The crystal structure of WT D-DT (PDB entry: 1DPT) served as the search model for L117G (PDB entry: 8VFO).

In light of these findings, we induced backbone flexibility by introducing Gly mutations. Single (L117G), double (L117G/F116G), triple (L117G/F116G/T115G), and quadruple (L117G/F116G/T115G/M114G) Gly variants were produced, keeping the crystallographic findings of D-DT–4-CPPC in mind.³⁷

CD experiments for WT D-DT and the four Gly variants produced consistent profiles (Figure 5A). Kinetic analyses showed that the enhanced backbone flexibility of the C-terminal region did not significantly impact the K_M values of Gly variants, something that cannot be said for the k_{cat} and k_{cat}/K_M values (Figure 5B–D, Table S1). To couple the kinetic findings with structural insights, we performed MD simulations and analyzed the dynamic profiles of these variants. From the single (L117G) to quadruple (L117G/F116G/T115G/M114G) variant, we noted a gradual increase of the C-terminal's flexibility (Figure 5E). The extent (number of residues being affected) and magnitude (RMSF value) of this flexibility are directly correlated to the number of Gly residues being introduced. For example, in the case of L117G, high conformational flexibility was noted for C-terminal residues Met114–Leu117. When three additional amino acids are mutated to Gly, the number of residues drastically affected increases to 11 (Ile107–Leu117). Interestingly, this enhanced flexibility of the C-terminal region does not have a noticeable effect on the α_1/β_2 and β_4/α_2 loops, which are found in proximity (Figure 5E). This can only be explained by accepting that the flexible segment of the C-terminal residues spans outward from the biological assembly of D-DT to the solvent.

L117G was also crystallized, and its structural features were analyzed (Table S7). The rmsd value was 0.46 Å (Table S4), which was obtained by superposing L117G onto WT D-DT, and shows that the two crystal structures have an overall satisfactory agreement with an exception to the C-terminal region (Figure 5F). In agreement with the MD simulations, the single point mutation of Leu117 to Gly amplified the flexibility of residues 114–117 (Figure 5E). Phe116 and C-terminus Leu117 lacked electron density, while Met114 and Thr115 adopted a distinctively structural conformation from the corresponding amino acids of WT D-DT (Figure 5F). Of great interest is the effect of L117G on Val113. According to the crystallographic findings, the side chain of Val113 remains “locked” in the hydrophobic pocket formed between the α_2 helix and the C-terminal 3.6 helix (Figure 5F). This finding evidently shows that the conformational flexibility of the C-terminal region, which is induced by the Gly mutation, extends toward the solvent without affecting the biological assembly of D-DT.

Characterization of the C-Terminal Truncation Variants. To complete our investigation, we designed, expressed, and purified three C-terminal truncation variants of D-DT: $\Delta 114$ – 117 , $\Delta 109$ – 117 , and $\Delta 104$ – 117 . Considering the potentially detrimental effect of truncations on protein folding, we first performed CD experiments and analyzed the data side-by-side with WT D-DT. Our findings demonstrated negligible differences across the four samples (Figure 6A). Similar to the Ala and Gly mutants, we then carried out kinetic experiments to explore the impact of C-terminal truncation on

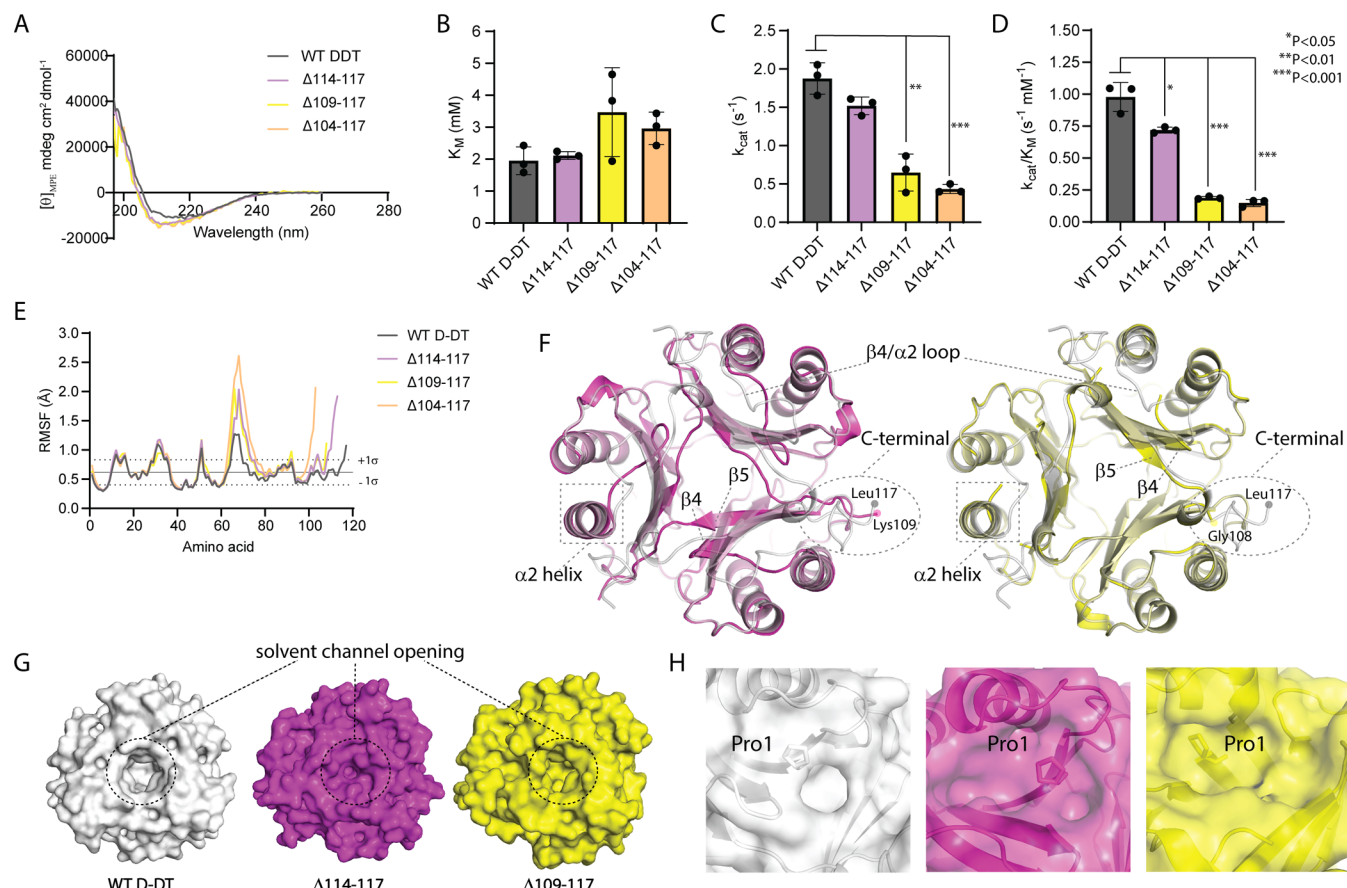


Figure 6. Structural and functional analysis of C-terminal truncation variants. (A) The folding profiles of WT D-DT, Δ114–117, Δ109–117, and Δ104–117 were examined by CD spectroscopy. (B–D) Bar-chat analysis of the Michaelis–Menten parameters for WT D-DT and the C-terminal truncation variants. The experiments were carried out in triplicate ($n = 3$) and the error values are shown as standard deviations. (E) RMSF profiles of WT D-DT, Δ114–117, Δ109–117, and Δ104–117. The black dashed lines represent one standard deviation ($\pm 1\sigma$) from the mean value of WT D-DT (black solid line). (F) The crystal structures of Δ114–117 (left, magenta) and Δ109–117 (right, yellow) were superposed onto the corresponding structure of WT D-DT (transparent light gray). Structural differences at the α 2 helix, β 4/ α 2 loop, β 4 and β 5 strands, and C-terminal region are highlighted. The C-terminus residues of WT D-DT, Δ114–117, Δ109–117 are pointed with filled circles. (G) Conformational changes in the β 4 and β 5 strands alter the opening of the solvent channel (black dashed circles). (H) The C-terminal truncations modify the active site opening and volume, impacting, to some extent, the accessibility of the catalytic residue Pro1 (sticks). The crystal structure of WT D-DT (PDB entry: 1DPT) served as the search model for Δ114–117 (PDB entry: 8VDY) and Δ109–117 (8VFK).

the K_M , k_{cat} , and k_{cat}/K_M values of D-DT. Based on our findings, the K_M values of Δ114–117, Δ109–117, and Δ104–117 did not show a significant deviation from the corresponding value of WT D-DT (Figure 6B, Table S1). In contrast, the turnover number displayed a clear reduction, with Δ109–117 and Δ104–117 being affected the most. While Δ114–117 reduced its k_{cat} value by only 19%, Δ109–117 and Δ104–117 exhibited the corresponding drops of 65 and 77% (Figure 6C, Table S1). On the same trend with the k_{cat} values, the catalytic efficiency reduced from WT D-DT to Δ104–117. With WT D-DT as the point of reference, Δ109–117 and Δ104–117 revealed a sharp decline in their k_{cat}/K_M values by 81% and 85%, respectively (Figure 6D, Table S1). RMSF analysis of WT D-DT and the three truncation variants showed diverse dynamic profiles on the C-terminal region and residues 63–79, which are located on the β 4/ α 2 loop (residues 63–69) and α 2 helix (residues 70–79) (Figure 6E, Table S2). As shown by our data, the conformational flexibility at this region is variant dependent. Residues 70–79 were affected due to their proximity to the C-terminal tail of the adjacent monomer. An increase in the conformational flexibility of residues 70–79, in turn, promotes the conformational flexibility of the β 4/ α 2

loop. Due to the low catalytic efficiency of the truncation variants, inhibition studies were not an option. For this reason, we utilized matrix-assisted laser desorption/ionization time-of-flight mass spectrometry (MALDI-TOF MS) to probe pyridine-2,5-dicarboxylate binding. Of note, MALDI-TOF MS has been successfully used in protein–ligand studies and it is applicable even for high-throughput screening projects.⁴⁰ Following this approach, WT D-DT, Δ114–117, and Δ109–117 were experimentally analyzed showing that only WT D-DT and Δ114–117 bind the inhibitor (Figure S8).

Upon the crystallization of Δ114–117 and Δ109–117, we examined their structural features (Table S8). Superposition analyses of Δ114–117 and Δ109–117 onto WT D-DT yielded the corresponding rmsd values of 1.11 and 0.54 Å (Table S4). Between them, Δ114–117 and Δ109–117 yielded an rmsd value of 0.96 Å. The corresponding electron densities of Δ114–117 and Δ109–117 C-termini were clearly observed up to Lys109 (two out of three subunits) and Gly108 (all three subunits), respectively (Figure 6F). The structural disagreement, noted on superposing the two truncation variants onto WT D-DT, was mainly associated with conformational changes (observed in Δ114–117 and Δ109–117) and/or lack of

electron density (observed only in Δ109–117) at three regions: the α 2 helix, β 4/ α 2 loop, and C-terminus (Figure 6F). Due to the increased flexibility of the C-terminal tail, two out of the three subunits of Δ109–117 lacked the electron density of residues found on the α 2 helix and/or β 4/ α 2 loop. The enhanced mobility of the β 4/ α 2 loop and C-terminal region also impacted portions of the β 4 and β 5 strands, changing their conformations (Figure 6F). The conformational changes observed on the β 5 strand altered the opening of the solvent channel, as shown by the comparison of WT D-DT with the two variants (Figure 6G). To associate the crystallography findings of Δ114–117 and Δ109–117 with our original hypothesis (Figure S2), we also examined the surface surrounding the active site. Δ114–117 and Δ109–117 revealed noticeable differences from WT D-DT, as well as distinctions between them (Figure 6H). These differences are evident in the opening and volume of active site as well as the accessibility of the catalytic residue Pro1. Although both Δ114–117 and Δ109–117 increased their active site openings, the volume of the cavity was altered in a distinct way, impacting the accessibility of Pro1 (Figure 6H). In Δ114–117, Pro1 appears accessible comparable to WT D-DT. In contrast, Δ109–117 presents Pro1 in a conformation that does not favor catalysis. Together, these observations explain the catalytic findings of Δ114–117 and Δ109–117 (Figure 6B–D).

CONCLUSIONS

Previous studies focused on MIF^{41,42} reported that the C-terminal region has a key role in stabilizing the protein's tertiary structure as well as modulating the enzymatic activity. These conclusions were attributed to the ability of C-terminal residues to form intersubunit interactions that are important for stabilizing the biological assembly of MIF. More recent studies have shown that this region also has a functional role in the MIF-induced activation of CD74.^{23,24} While these studies enriched our understanding of MIF's structure and function, the corresponding analyses of its human homologue, D-DT, are yet to be reported.

Using a systematic approach, we probed understanding of the role of the C-terminal region in D-DT functionality. Seventeen protein variants were interrogated with high-resolution protein crystallography, biophysical assays, turnover and inhibition experiments, MD simulations, and mass spectrometry, yielding previously unseen structural features of D-DT that control protein–ligand recognition. Conformational changes of Thr115 serve a key role in the catalytic tautomerization of 4-HPP. Although the binding affinity of 4-HPP is not influenced, threonine-induced movements of the C-terminal region assign distinct conformations to residues that control the opening of the active site; primarily to Arg36. Upon altering the opening of the active site, accommodation of substrate and product release becomes more effective, something that is evident by the impressive k_{cat} and k_{cat}/K_M values of T115A.

For the first time, Arg36 was observed to have multiple functional tasks. Besides regulating ligand admission in the pocket, it is capable of adopting diverse conformations in order to stabilize the protein–ligand complex. This was experimentally observed twice in the crystal structures of T115A–4-CPPC and V113N–4-CPPC. Conformational changes of Arg36, as viewed by the crystal structure of V113N–4-CPPC, protect the protein–ligand complex from the harsh

dynamic events occurring proximal to the binding site. Notably, the diverse functionality of Arg36 is regulated by the conformational flexibility of the C-terminal region.

Val113, found in the hydrophobic pocket formed between helix α 2 and 3.6 helix C, appears to be a key residue for controlling the mobility of the C-terminal region. Mutation of Val to Asn displaces residue 113 from its hydrophobic pocket and increases the flexibility of the C-terminal residues. Although this region is not inherently flexible, the induced flexibility of the C-terminus by Asn113 can negatively affect catalysis via altering the conformational flexibility of the α 2 helix and β 4/ α 2 loop. A highly dynamic C-terminal tail primarily affects the α 2 helix of the adjacent monomer due to their proximity. Consequently, the β 4/ α 2 loop elevates its dynamic activity, influencing ligand binding and/or catalysis (e.g., active site opening, volume, and accessibility of Pro1). Future studies focused on elucidating the catalytic mechanism of 4-HPP tautomerization would further explain the effect of C-terminal variants in the k_{cat} and K_M values, while QM/MM calculations may add value by exposing any potential transition states.⁴³

Collectively, our work offers the first comprehensive analysis of the structural features that regulate molecular recognition in D-DT and may be used to better understand the catalytic mechanism of this protein as well as to promote drug discovery efforts.

EXPERIMENTAL SECTION

General Procedures. Production of D-DT variants was accomplished following the QuikChange site-directed mutagenesis protocol (Agilent Technologies, Santa Clara, CA). The DNA oligos used for mutagenesis are described in the Supporting Information (Table S9). With the exception of L117G/F116G/T115G/M114G, all the remaining variants were synthesized using pET-22b(+)–WT D-DT as a template. The quadruple glycine mutant was produced, utilizing pET-22b(+)–L117G/F116G/T115G as a template. The polymerase chain reaction (PCR) products were digested with Dpn I (New England Biolabs) and transformed into XL10-Gold ultracompetent cells (Agilent Technologies, Santa Clara, CA). All D-DT variants were confirmed by sequencing. Protein purity was analyzed by sodium dodecyl sulfate–polyacrylamide gel electrophoresis (SDS-PAGE). Protein concentration was determined by the Pierce BCA Protein Assay Kit (Thermo Fisher Scientific) following the manufacturer's protocol. CD experiments were carried out in a JASCO J-815 spectropolarimeter. The mass spectrometry experiments were performed in a Kratos-Shimadzu Axima-CFR MALDI-TOF mass spectrometer. Kinetic assays were carried out in a Tecan Infinite M-Plex microplate reader.

Materials. All solvents and chemicals were of the highest analytical grade and used without further purification. 4-HPP (>95% purity) was purchased from TCI America. 4-CPPC (99% purity) was obtained from Axon Medchem. Sinapinic acid (>99% purity) was bought from Fluka. Dimethyl sulfoxide (DMSO) and Luria Broth (LB) media were purchased from VWR. Polyethylene glycol (PEG) 3350 and 4000 were obtained from Sigma-Aldrich and TCI America, respectively. Isopropyl β -D-1-thiogalactopyranoside (IPTG) and ampicillin sodium salt were purchased from Gold Biotechnology. All tools and consumables required for protein crystallography were purchased from Hampton Research.

Protein Expression and Purification. The D-DT variants were expressed and purified in a similar manner as previously described.^{32,39} The plasmid encoding the protein of interest was transformed into BL21(DE3) competent *E. coli* cells (Agilent Technologies). The cells were then grown in 1 L of LB media enriched with 100 μ g/mL of ampicillin, under shaking at 37 °C, until they reached an optical density at 600 nm (OD_{600}) of 0.6–0.8. At this point, protein expression was induced by the addition of 1 mM IPTG,

and the cells were incubated for an additional 4 h at the same temperature. The cells were then collected by centrifugation, washed with the lysis buffer (20 mM Tris HCl pH 8.5, 20 mM NaCl), and stored in 50 mL centrifuge tubes. Cell pellets of the poly glycine mutants were lysed in the lysis buffer adjusted to pH 8.0, while all the remaining variants, including WT D-DT, were lysed in the regular lysis buffer (20 mM Tris HCl pH 8.5, 20 mM NaCl). WT D-DT, single-point alanine mutants, V113 mutants, and poly glycine variants were loaded onto a 5 mL Q-Sepharose column that was equilibrated in their respective lysis buffers. The poly glycine variants came off in the flow-through after the lysate peak, meanwhile WT D-DT and the other variants bound to the column and eluted with 5% of the elution buffer (20 mM Tris HCl pH 8.5, 1 M NaCl). The truncation variants were loaded onto a 5 mL Q-Sepharose column connected in series to a 120 mL Q-Sepharose column. Once the protein was loaded, 10% of the elution buffer was introduced, and the protein came off in the flow though. In all cases, fractions containing the protein of interest were collected, and concentrated for further purification by size exclusion chromatography (SEC) using a 16/60 Superdex 75 column (Cytiva, Marlborough, MA). For this step, 20 mM Tris HCl pH 7.4, 20 mM NaCl was always used as a running buffer. Monodisperse fractions containing >95% pure protein were collected, concentrated, and stored at -80 °C for further use.

Circular Dichroism Spectroscopy. All experiments were performed in a 1 mm quartz cuvette, while the folding profiles of D-DT variants (20 μ M) were recorded between 260 and 195 nm, as described before.²⁶ Prior to each experiment, the running buffer composed of 20 mM sodium phosphate at pH 7.0 and 1 mM EDTA was degassed with ultrahigh purity nitrogen. The triplicate data sets were analyzed in GraphPad Prism 10.

Kinetic Experiments. Keto-enol tautomerase assays were performed in a similar manner to what has been previously published.³¹ Briefly, a 30 mM stock of 4-HPP stock was prepared in 0.5 M ammonium acetate, pH 6.2 (4-HPP buffer), and incubated overnight at room temperature while rocking. The stock was then diluted with the 4-HPP buffer to create a final concentration range of 0–2 mM. The substrate solution was added to a 96-well microplate, and a borate solution with a working concentration of 0.42 M was introduced. The reaction was then initiated by the addition of protein at a final concentration of 250 nM. Formation of the enol–borate complex ($\epsilon_{306} = 11,400 \text{ M}^{-1} \text{ cm}^{-1}$) was monitored at 306 nm, for 300 s and having 10 s intervals. The data was analyzed using GraphPad Prism 10. All experiments were performed in triplicate.

Protein Crystallization. Crystallization of D-DT variants was performed in 24-well hanging drop plates. All proteins were concentrated to 12 mg/mL except for T115A, which was concentrated to 10 mg/mL. Proteins and mother liquor were mixed in a 1:1 (v/v) ratio. The crystallization conditions of D-DT variants are as follows: WT D-DT: 24–30% PEG 4000, 0.1 M sodium citrate pH 5.6–6.0, 0.2 M ammonium acetate; V113N: 26–32% PEG 4000, 0.1 M sodium citrate pH 5.2–5.8, 0.2 M ammonium acetate; Δ 114–117: 26–32% PEG 3350, 0.25–0.275 M ammonium acetate; Δ 109–117: 26–28% PEG 4000, 0.1 M sodium citrate pH 6.0–6.2, 0.2 M ammonium acetate; T115A: 28–30% PEG 4000, 0.1 M sodium citrate pH 5.8–6.2, 0.2 M ammonium acetate. Crystals, which varied in shape, were formed at different time points and reached their full size within 2 weeks. Co-crystal structures of D-DT variants with the selective inhibitor 4-CPPC were acquired by soaking the apo crystals into pre-equilibrated drops of mother liquor enriched with 100 mM 4-CPPC. Similar to what had been previously used,³⁷ the high concentration of PEG 4000 served as the cryoprotectant for the D-DT crystals.

X-ray Data Collection and Crystal Structure Determination. Single-crystal X-ray diffraction data was collected by the Advanced Light Source (ALS) beamline 8.3.1 (wavelength of 1.11583 Å) of the Lawrence Berkeley National Lab, which is equipped with a Dectris Pilatus3 S 6 M detector. Data reduction was carried out using DIALS⁴⁴ as implemented via the xia2 software package.⁴⁵ The crystal structures of D-DT variants were obtained via molecular replacement using the CCP4-supported program, Molrep.⁴⁶ In all cases, WT D-DT

(PDB entry: 1DPT) served as the search structure. After obtaining the initial model, each variant underwent further refinement using Refmac5⁴⁷ and COOT,⁴⁸ while the structures were visualized in PyMOL.⁴⁹ 4-CPPC coordinates and crystallographic information file (CIF) were generated by the CCP4-supported program, PRODRG.⁵⁰ rmsd of finalized crystal structures were determined by Superpose (CCP4 supported). In the cases of V113N, Δ 114–117, and Δ 109–117, rmsd calculations were performed per monomer to obtain the most accurate alignment and averaged in order to obtain the final values for the homotrimeric assembly. The crystallographic tables are provided in the Supporting Information. Ramachandran analyses showed 0% outliers and all residues in the favored regions.

MALDI-TOF MS Analysis. All experiments were carried out in linear mode with a 120 cm flight tube in a turbo molecular vacuum of approximately 10⁻⁶ Torr. For ionization, an N₂-laser (λ = 337 nm, 120 mJ/pulse) was used along with manual X-Y-stage adjustment for optimal ion formation. The laser attenuator was adjusted to a threshold where ion formation was just beginning. Ions were extracted with a potential of 20 kV after a 350 ns collisional cooling delay. For instrument calibration, protein standards were used (ProteoMass, Sigma-Aldrich). The calibration sample (1 μ L, 20 pmol of each protein) was crystallized on the plate with sinapinic acid (2 mg/mL in MeCN/0.1% TFA 1:1, 1 μ L). The same matrix was used for analysis of D-DT protein samples whose concentrations were at 40 μ g/mL (1 μ L spotted = 40 ng of protein, approximately 3–5 pmol on the plate). Data files were processed with Shimadzu Biotech Launchpad software (ver. 2.9.3.2011624). Both calibration spectra and experimental spectra were smoothed to show average *m/z* values of all ion peaks.

MD Simulations. MD simulations were carried out similarly to what was previously described.^{26,38} All structures for the simulations were prepared from the WT D-DT structure (PDB entry: 1DPT). The additional, nonprotein atoms were first removed from the structure and the biological assembly was generated using PyMOL. Mutations and truncations were made using UCSF Chimera.⁵¹ The structures were used as inputs for psfgen, a VMD plug-in,⁵² to generate a new PDB/PSF pair containing hydrogens. The PSFs and PDBs for each structure were input into VMD's solvate plug-in to create another PSF/PDB pair with the protein inside a water box. The charge of the system was checked and balanced using the autoionize plug-in. Each system was minimized, heated to 300 K, and equilibrated before the 200 ns production run. The RMSF data of the α -carbons was produced by GROMACS.⁵³ The simulations and subsequent analyses were performed in duplicate.

Statistics. The experiments shown in this study were performed in triplicate unless otherwise stated. Error is shown as the \pm SD (standard deviation) from the mean value. Statistical analysis was performed using the unpaired *t*-test (GraphPad Prism 10), while statistical significance is expressed as **p* < 0.05, ***p* < 0.01, ****p* < 0.001.

ASSOCIATED CONTENT

Supporting Information

The Supporting Information is available free of charge at <https://pubs.acs.org/doi/10.1021/acs.jmedchem.4c00177>.

Steady-state kinetic parameters, RMSF, and rmsd analyses, crystallographic tables, and DNA oligo sequences; crystallographic analyses, modeling, kinetic analyses, and mass spectrometry data; and PDB files generated for the three D-DT truncation models (Δ 114–117, Δ 109–117, and Δ 104–117) (PDF)

Δ 114–117 model (PDB)

Δ 109–117 model (PDB)

Δ 104–117 model (PDB)

Accession Codes

PDB ID of New Crystal (X-ray) Structures: The final models for all variants have been deposited in RCSB Protein Data Bank (RCSB PDB) with the following identification numbers:

WT D-DT at 290 K (8VFL), WT D-DT at 310 K (8VFN), T115A (8VG7), T115A-4-CPPC (8VG8), V113N (8VFW), V113N-4-CPPC (8VG5), L117G (8VFO), Δ114-117 (8VDY), and Δ109-117 (8VFK). Authors will release the atomic coordinates upon article publication.

AUTHOR INFORMATION

Corresponding Author

Georgios Pantouris — Department of Chemistry, University of the Pacific, Stockton, California 95211, United States;
orcid.org/0000-0001-5547-1406; Email: gpantouris@pacific.edu

Authors

Andrew Parkins — Department of Chemistry, University of the Pacific, Stockton, California 95211, United States

Aliyah Veronica R. Pilien — Department of Chemistry, University of the Pacific, Stockton, California 95211, United States

Alexander M. Wolff — Department of Chemistry and Biochemistry, University of California, Merced, California 95340, United States

Christopher Argueta — Department of Chemistry, University of the Pacific, Stockton, California 95211, United States

Jasmine Vargas — Department of Chemistry, University of the Pacific, Stockton, California 95211, United States

Shahrzad Sadeghi — Department of Chemistry, University of the Pacific, Stockton, California 95211, United States;
orcid.org/0009-0009-2420-6920

Andreas H. Franz — Department of Chemistry, University of the Pacific, Stockton, California 95211, United States

Michael C. Thompson — Department of Chemistry and Biochemistry, University of California, Merced, California 95340, United States

Complete contact information is available at:

<https://pubs.acs.org/10.1021/acs.jmedchem.4c00177>

Author Contributions

A.P. and A.V.R.P. are equally contributing authors. All authors have given approval to the final version of the manuscript.

Notes

The authors declare no competing financial interest.

ACKNOWLEDGMENTS

This work was supported by funds from the Chemistry Department, University of the Pacific and Scholarly/Artistic Activities grant (G.P.). The TOC figure was created with BioRender.com under paid subscription.

ABBREVIATIONS

4-CPPC, 4-(3-carboxyphenyl)-2,5-pyridinedicarboxylic acid; 4-HPP, 4-hydroxylphenylpyruvate; ACKR-3, atypical chemokine receptor-3; ALS, Advanced Light Source; AMPK, Adenosine monophosphate activated protein kinase; Akt, protein kinase B; CD, circular dichroism; CD74, cluster of differentiation 74; COX2, cyclooxygenase 2; CIF, crystallographic information file; D-DT, D-dopachrome tautomerase; DHI, 5,6-dihydroxyindole; EDTA, ethylenediamine tetraacetic acid; ERK, extracellular signal-regulated kinase; IPTG, Isopropyl β -D-1-thiogalactopyranoside; LB, Luria-broth; MALDI-TOF MS, matrix-assisted laser desorption/ionization time-of-flight mass spectrometry; MAPK, mitogen-activated protein kinase; MD,

molecular dynamics; MeCN, Acetonitrile; MIF, macrophage migration inhibitory factor; NF- κ B, nuclear factor kappa B; NMR, nuclear magnetic resonance; NSCLC, nonsmall cell lung cancer; PCR, polymerase chain reaction; PDB, Protein Data Bank; PEG, polyethylene glycol; PGE₂, Prostaglandin E2; PI3K, phosphoinositide 3-kinase; PSF, protein structure file; rmsd, root mean squared deviation; RMSF, root mean squared fluctuation; SEC, size exclusion chromatography; TFA, trifluoroacetic acid; WT, wild type

REFERENCES

- (1) Merk, M.; Zierow, S.; Leng, L.; Das, R.; Du, X.; Schulte, W.; Fan, J.; Lue, H.; Chen, Y.; Xiong, H.; et al. The D-dopachrome tautomerase (DDT) gene product is a cytokine and functional homolog of macrophage migration inhibitory factor (MIF). *Proc. Natl. Acad. Sci. U.S.A.* **2011**, *108* (34), No. E577–E585.
- (2) Nishihira, J.; Fujinaga, M.; Kuriyama, T.; Suzuki, M.; Sugimoto, H.; Nakagawa, A.; Tanaka, I.; Sakai, M. Molecular cloning of human D-dopachrome tautomerase cDNA: N-terminal proline is essential for enzyme activation. *Biochem. Biophys. Res. Commun.* **1998**, *243* (2), 538–544.
- (3) Zan, C.; Yang, B.; Brandhofer, M.; El Bounkari, O.; Bernhagen, J. D-dopachrome tautomerase in cardiovascular and inflammatory diseases—A new kid on the block or just another MIF? *FASEB J.* **2022**, *36* (11), No. e22601.
- (4) Jankauskas, S. S.; Wong, D. W. L.; Bucala, R.; Djudjaj, S.; Boor, P. Evolving complexity of MIF signaling. *Cell. Signalling* **2019**, *57*, 76–88.
- (5) Xiao, Z.; Chen, D.; Mulder, F.; Song, S.; van der Wouden, P. E.; Cool, R. H.; Melgert, B. N.; Poelarends, G. J.; Dekker, F. J. 4-Iodopyrimidine Labeling Reveals Nuclear Translocation and Nuclease Activity for Both MIF and MIF2. *Chemistry* **2022**, *28* (1), No. e202103030.
- (6) Odh, G.; Hindemith, A.; Rosengren, A. M.; Rosengren, E.; Rorsman, H. Isolation of a new tautomerase monitored by the conversion of D-dopachrome to 5,6-dihydroxyindole. *Biochem. Biophys. Res. Commun.* **1993**, *197* (2), 619–624.
- (7) Sugimoto, H.; Taniguchi, M.; Nakagawa, A.; Tanaka, I.; Suzuki, M.; Nishihira, J. Crystal structure of human D-dopachrome tautomerase, a homologue of macrophage migration inhibitory factor, at 1.54 Å resolution. *Biochemistry* **1999**, *38* (11), 3268–3279.
- (8) Tilstam, P. V.; Schulte, W.; Holowka, T.; Kim, B. S.; Nouws, J.; Sauler, M.; Piecychna, M.; Pantouris, G.; Lolis, E.; Leng, L.; et al. MIF but not MIF-2 recruits inflammatory macrophages in an experimental polymicrobial sepsis model. *J. Clin. Invest.* **2021**, *131* (23), No. e127171.
- (9) Stoppe, C.; Rex, S.; Goetzenich, A.; Kraemer, S.; Emontzpolh, C.; Soppert, J.; Averdunk, L.; Sun, Y.; Rossaint, R.; Lue, H.; et al. Interaction of MIF Family Proteins in Myocardial Ischemia/Reperfusion Damage and Their Influence on Clinical Outcome of Cardiac Surgery Patients. *Antioxid. Redox Signaling* **2015**, *23* (11), 865–879.
- (10) Guo, D.; Guo, J.; Yao, J.; Jiang, K.; Hu, J.; Wang, B.; Liu, H.; Lin, L.; Sun, W.; Jiang, X. D-dopachrome tautomerase is over-expressed in pancreatic ductal adenocarcinoma and acts cooperatively with macrophage migration inhibitory factor to promote cancer growth. *Int. J. Cancer* **2016**, *139* (9), 2056–2067.
- (11) Leng, L.; Metz, C. N.; Fang, Y.; Xu, J.; Donnelly, S.; Baugh, J.; Delohery, T.; Chen, Y.; Mitchell, R. A.; Bucala, R. MIF signal transduction initiated by binding to CD74. *J. Exp. Med.* **2003**, *197* (11), 1467–1476.
- (12) Shi, X.; Leng, L.; Wang, T.; Wang, W.; Du, X.; Li, J.; McDonald, C.; Chen, Z.; Murphy, J. W.; Lolis, E.; et al. CD44 is the signaling component of the macrophage migration inhibitory factor-CD74 receptor complex. *Immunity* **2006**, *25* (4), 595–606.
- (13) Alampour-Rajabi, S.; El Bounkari, O.; Rot, A.; Müller-Newen, G.; Bachelerie, F.; Gawaz, M.; Weber, C.; Schober, A.; Bernhagen, J. MIF interacts with CXCR7 to promote receptor internalization,

- ERK1/2 and ZAP-70 signaling, and lymphocyte chemotaxis. *FASEB J.* **2015**, *29* (11), 4497–4511.
- (14) Song, S.; Liu, B.; Habibie, H.; van den Bor, J.; Smit, M. J.; Gosens, R.; Wu, X.; Brandsma, C. A.; Cool, R. H.; Haisma, H. J.; et al. D-dopachrome tautomerase contributes to lung epithelial repair via atypical chemokine receptor 3-dependent Akt signaling. *EBioMedicine* **2021**, *68*, 103412.
- (15) Weber, C.; Kraemer, S.; Drechsler, M.; Lue, H.; Koenen, R. R.; Kapurniotu, A.; Zernecke, A.; Bernhagen, J. Structural determinants of MIF functions in CXCR2-mediated inflammatory and atherogenic leukocyte recruitment. *Proc. Natl. Acad. Sci. U.S.A.* **2008**, *105* (42), 16278–16283.
- (16) Bernhagen, J.; Krohn, R.; Lue, H.; Gregory, J. L.; Zernecke, A.; Koenen, R. R.; Dewor, M.; Georgiev, I.; Schober, A.; Leng, L.; et al. MIF is a noncognate ligand of CXC chemokine receptors in inflammatory and atherogenic cell recruitment. *Nat. Med.* **2007**, *13* (5), 587–596.
- (17) Kontos, C.; El Bounkari, O.; Krammer, C.; Sinitski, D.; Hille, K.; Zan, C.; Yan, G.; Wang, S.; Gao, Y.; Brandhofer, M.; et al. Designed CXCR4 mimic acts as a soluble chemokine receptor that blocks atherogenic inflammation by agonist-specific targeting. *Nat. Commun.* **2020**, *11* (1), 5981.
- (18) Lacy, M.; Kontos, C.; Brandhofer, M.; Hille, K.; Groning, S.; Sinitski, D.; Bourilhon, P.; Rosenberg, E.; Krammer, C.; Thavayogarajah, T.; et al. Identification of an Arg-Leu-Arg tripeptide that contributes to the binding interface between the cytokine MIF and the chemokine receptor CXCR4. *Sci. Rep.* **2018**, *8* (1), 5171.
- (19) Ishimoto, K.; Iwata, T.; Taniguchi, H.; Mizusawa, N.; Tanaka, E.; Yoshimoto, K. D-dopachrome tautomerase promotes IL-6 expression and inhibits adipogenesis in preadipocytes. *Cytokine* **2012**, *60* (3), 772–777.
- (20) Li, H.; He, B.; Zhang, X.; Hao, H.; Yang, T.; Sun, C.; Song, H.; Wang, Y.; Zhou, Y.; Zhu, Z.; et al. D-dopachrome tautomerase drives astroglial inflammation via NF-κB signaling following spinal cord injury. *Cell Biosci.* **2022**, *12* (1), 128.
- (21) Ji, H.; Zhang, Y.; Chen, C.; Li, H.; He, B.; Yang, T.; Sun, C.; Hao, H.; Zhang, X.; Wang, Y.; et al. D-dopachrome tautomerase activates COX2/PGE(2) pathway of astrocytes to mediate inflammation following spinal cord injury. *J. Neuroinflammation* **2021**, *18* (1), 130.
- (22) Qi, D.; Atsina, K.; Qu, L.; Hu, X.; Wu, X.; Xu, B.; Piecychna, M.; Leng, L.; Fingerle-Rowson, G.; Zhang, J.; et al. The vestigial enzyme D-dopachrome tautomerase protects the heart against ischemic injury. *J. Clin. Invest.* **2014**, *124* (8), 3540–3550.
- (23) Pantouris, G.; Syed, M. A.; Fan, C.; Rajasekaran, D.; Cho, T. Y.; Rosenberg, E. M., Jr.; Bucala, R.; Bhandari, V.; Lolis, E. J. An Analysis of MIF Structural Features that Control Functional Activation of CD74. *Chem. Biol.* **2015**, *22* (9), 1197–1205.
- (24) Pantouris, G.; Ho, J.; Shah, D.; Syed, M. A.; Leng, L.; Bhandari, V.; Bucala, R.; Batista, V. S.; Loria, J. P.; Lolis, E. J. Nanosecond Dynamics Regulate the MIF-Induced Activity of CD74. *Angew. Chem., Int. Ed. Engl.* **2018**, *57* (24), 7116–7119.
- (25) Pantouris, G.; Khurana, L.; Ma, A.; Skeens, E.; Reiss, K.; Batista, V. S.; Lisi, G. P.; Lolis, E. J. Regulation of MIF Enzymatic Activity by an Allosteric Site at the Central Solvent Channel. *Cell Chem. Biol.* **2020**, *27* (6), 740.
- (26) Parkins, A.; Skeens, E.; McCallum, C. M.; Lisi, G. P.; Pantouris, G. The N-terminus of MIF regulates the dynamic profile of residues involved in CD74 activation. *Biophys. J.* **2021**, *120* (18), 3893–3900.
- (27) Skeens, E.; Pantouris, G.; Shah, D.; Manjula, R.; Ombrello, M. J.; Maluf, N. K.; Bhandari, V.; Lisi, G. P.; Lolis, E. J. A Cysteine Variant at an Allosteric Site Alters MIF Dynamics and Biological Function in Homo- and Heterotrimeric Assemblies. *Front. Mol. Biosci.* **2022**, *9*, 783669.
- (28) Chen, E.; Widjaja, V.; Kyro, G.; Allen, B.; Das, P.; Prahaladan, V. M.; Bhandari, V.; Lolis, E. J.; Batista, V. S.; Lisi, G. P. Mapping N-to C-terminal allosteric coupling through disruption of a putative CD74 activation site in D-dopachrome tautomerase. *J. Biol. Chem.* **2023**, *298* (6), 104729.
- (29) Chen, E.; Reiss, K.; Shah, D.; Manjula, R.; Allen, B.; Murphy, E. L.; Murphy, J. W.; Batista, V. S.; Bhandari, V.; Lolis, E. J.; et al. A structurally preserved allosteric site in the MIF superfamily affects enzymatic activity and CD74 activation in D-dopachrome tautomerase. *J. Biol. Chem.* **2021**, *297* (3), 101061.
- (30) Meza-Romero, R.; Benedek, G.; Jordan, K.; Leng, L.; Pantouris, G.; Lolis, E.; Bucala, R.; Vandenberg, A. A. Modeling of both shared and distinct interactions between MIF and its homologue D-DT with their common receptor CD74. *Cytokine* **2016**, *88*, 62–70.
- (31) Parkins, A.; Sandin, S. I.; Knittel, J.; Franz, A. H.; Ren, J.; de Alba, E.; Pantouris, G. Underrepresented Impurities in 4-Hydroxyphenylpyruvate Affect the Catalytic Activity of Multiple Enzymes. *Anal. Chem.* **2023**, *95* (11), 4957–4965.
- (32) Parkins, A.; Pantouris, G. Protocol for purification and enzymatic characterization of members of the human macrophage migration inhibitory factor superfamily. *STAR Protoc.* **2023**, *4* (3), 102375.
- (33) Xiao, Z.; Osipyan, A.; Song, S.; Chen, D.; Schut, R. A.; van Merkerk, R.; van der Wouden, P. E.; Cool, R. H.; Quax, W. J.; Melgert, B. N.; et al. Thieno[2,3-d]pyrimidine-2,4(1H,3H)-dione Derivative Inhibits D-Dopachrome Tautomerase Activity and Suppresses the Proliferation of Non-Small Cell Lung Cancer Cells. *J. Med. Chem.* **2022**, *65* (3), 2059–2077.
- (34) Winner, M.; Meier, J.; Zierow, S.; Rendon, B. E.; Crichlow, G. V.; Riggs, R.; Bucala, R.; Leng, L.; Smith, N.; Lolis, E.; et al. A novel, macrophage migration inhibitory factor suicide substrate inhibits motility and growth of lung cancer cells. *Cancer Res.* **2008**, *68* (18), 7253–7257.
- (35) Rajasekaran, D.; Zierow, S.; Syed, M.; Bucala, R.; Bhandari, V.; Lolis, E. J. Targeting distinct tautomerase sites of D-DT and MIF with a single molecule for inhibition of neutrophil lung recruitment. *FASEB J.* **2014**, *28* (11), 4961–4971.
- (36) Tilstam, P. V.; Pantouris, G.; Corman, M.; Andreoli, M.; Mahboubi, K.; Davis, G.; Du, X.; Leng, L.; Lolis, E.; Bucala, R. A selective small-molecule inhibitor of macrophage migration inhibitory factor-2 (MIF-2), a MIF cytokine superfamily member, inhibits MIF-2 biological activity. *J. Biol. Chem.* **2019**, *294* (49), 18522–18531.
- (37) Pantouris, G.; Bucala, R.; Lolis, E. J. Structural plasticity in the C-terminal region of macrophage migration inhibitory factor-2 is associated with an induced fit mechanism for a selective inhibitor. *Biochemistry* **2018**, *57* (26), 3599–3605.
- (38) Parkins, A.; Chen, E.; Rangel, V. M.; Singh, M.; Xue, L.; Lisi, G. P.; Pantouris, G. Ligand-induced conformational changes enable intersubunit communications in D-dopachrome tautomerase. *Biophys. J.* **2023**, *122*, 1268–1276.
- (39) Parkins, A.; Das, P.; Prahaladan, V.; Rangel, V. M.; Xue, L.; Sankaran, B.; Bhandari, V.; Pantouris, G. 2,5-Pyridinedicarboxylic acid is a bioactive and highly selective inhibitor of D-dopachrome tautomerase. *Structure* **2023**, *31* (3), 355.
- (40) Haslam, C.; Hellicar, J.; Dunn, A.; Fuetterer, A.; Hardy, N.; Marshall, P.; Paape, R.; Pemberton, M.; Resemannand, A.; Leveridge, M. The Evolution of MALDI-TOF Mass Spectrometry toward Ultra-High-Throughput Screening: 1536-Well Format and Beyond. *J. Biomol. Screening* **2016**, *21* (2), 176–186.
- (41) Mischke, R.; Gessner, A.; Kapurniotu, A.; Jüttner, S.; Kleemann, R.; Brunner, H.; Bernhagen, J. Structure activity studies of the cytokine macrophage migration inhibitory factor (MIF) reveal a critical role for its carboxy terminus. *FEBS Lett.* **1997**, *414* (2), 226–232.
- (42) El-Turk, F.; Cascella, M.; Ouertatani-Sakouhi, H.; Narayanan, R. L.; Leng, L.; Bucala, R.; Zweckstetter, M.; Rothlisberger, U.; Lashuel, H. A. The conformational flexibility of the carboxy terminal residues 105–114 is a key modulator of the catalytic activity and stability of macrophage migration inhibitory factor. *Biochemistry* **2008**, *47* (40), 10740–10756.
- (43) Beraud-Pache, R.; Garcia-Iriepa, C.; Navizet, I. Modeling Chemical Reactions by QM/MM Calculations: The Case of the Tautomerization in Fireflies Bioluminescent Systems. *Front. Chem.* **2018**, *6*, 116.

- (44) Winter, G.; Waterman, D. G.; Parkhurst, J. M.; Brewster, A. S.; Gildea, R. J.; Gerstel, M.; Fuentes-Montero, L.; Vollmar, M.; Michels-Clark, T.; Young, I. D.; et al. DIALS: implementation and evaluation of a new integration package. *Acta Crystallogr., Sect. D: Struct. Biol.* **2018**, *74* (2), 85–97.
- (45) Winter, G. xia2: an expert system for macromolecular crystallography data reduction. *J. Appl. Crystallogr.* **2010**, *43* (1), 186–190.
- (46) Winn, M. D.; Ballard, C. C.; Cowtan, K. D.; Dodson, E. J.; Emsley, P.; Evans, P. R.; Keegan, R. M.; Krissinel, E. B.; Leslie, A. G.; McCoy, A.; et al. Overview of the CCP4 suite and current developments. *Acta Crystallogr., Sect. D: Biol. Crystallogr.* **2011**, *67* (4), 235–242.
- (47) Murshudov, G. N.; Skubák, P.; Lebedev, A. A.; Pannu, N. S.; Steiner, R. A.; Nicholls, R. A.; Winn, M. D.; Long, F.; Vagin, A. A. REFMACS for the refinement of macromolecular crystal structures. *Acta Crystallogr., Sect. D: Biol. Crystallogr.* **2011**, *67* (4), 355–367.
- (48) Emsley, P.; Cowtan, K. Coot: model-building tools for molecular graphics. *Acta Crystallogr., Sect. D: Biol. Crystallogr.* **2004**, *60* (12), 2126–2132.
- (49) DeLano, W. L. *The PyMOL Molecular Graphics System*; Delano Scientific: San Carlos, 2002.
- (50) Schuttelkopf, A. W.; van Aalten, D. M. PRODRG: a tool for high-throughput crystallography of protein-ligand complexes. *Acta Crystallogr., Sect. D: Biol. Crystallogr.* **2004**, *60* (8), 1355–1363.
- (51) Pettersen, E. F.; Goddard, T. D.; Huang, C. C.; Couch, G. S.; Greenblatt, D. M.; Meng, E. C.; Ferrin, T. E. UCSF Chimera—a visualization system for exploratory research and analysis. *J. Comput. Chem.* **2004**, *25* (13), 1605–1612.
- (52) Humphrey, W.; Dalke, A.; Schulten, K. VMD: visual molecular dynamics. *J. Mol. Graphics* **1996**, *14* (1), 33–38.
- (53) Van Der Spoel, D.; Lindahl, E.; Hess, B.; Groenhof, G.; Mark, A. E.; Berendsen, H. J. GROMACS: fast, flexible, and free. *J. Comput. Chem.* **2005**, *26* (16), 1701–1718.